Geophysical Research Letters

RESEARCH LETTER
10.1029/2023GL103813

Key Points:

- Slab tearing occurs along an ancient fracture zone in the subducted Phoenix plate
- Active magmatic underplating could trigger the Orca earthquake swarm

Supporting Information:

Supporting Information may be found in the online version of this article.

Correspondence to:

J. A. Parera-Portell,
jpareraportell@ugr.es

Citation:

Parera-Portell, J. A., Mancilla, F. D. L., Almendros, J., Morales, J., & Stich, D. (2023). Slab tearing underneath the Bransfield Strait, Antarctica. *Geophysical Research Letters*, *50*, e2023GL103813. https://doi.org/10.1029/2023GL103813

Received 22 MAR 2023
Accepted 27 JUN 2023

Author Contributions:

Conceptualization: F. D. L. Mancilla
Formal analysis: J. A. Parera-Portell, D. Stich
Investigation: J. A. Parera-Portell, F. D. L. Mancilla, J. Morales
Project Administration: J. Almendros
Resources: J. Almendros
Software: J. A. Parera-Portell
Supervision: F. D. L. Mancilla, J. Almendros
Visualization: J. A. Parera-Portell
Writing – original draft: J. A. Parera-Portell
Writing – review & editing: F. D. L. Mancilla, J. Almendros, J. Morales, D. Stich

Slab Tearing Underneath the Bransfield Strait, Antarctica

J. A. Parera-Portell[1,2], F. D. L. Mancilla[1,2], J. Almendros[1,2], J. Morales[1,2], and D. Stich[1,2]

[1]Instituto Andaluz de Geofísica, Universidad de Granada, Granada, Spain, [2]Departamento de Física Teórica y del Cosmos, Universidad de Granada, Granada, Spain

Abstract We conduct a P-wave receiver function analysis of the Bransfield Strait (West Antarctica) to determine the lithospheric structure of this back-arc basin, thanks to 31 temporary and permanent stations. Our main finding is a 15 km tear of the Phoenix slab, coinciding with the location of the 2020–2021 Orca earthquake swarm's epicenters. Teleseismic wave modeling reveals that the two major earthquakes occurred at the base of the crust, suggesting that the swarm could have been triggered by active underplating driven by mantle flow through the slab tear. There is evidence for such an underplating layer at least under Deception Island and for a widespread low velocity zone in the mantle wedge probably undergoing partial melting. We found average crustal thickness (30.5 ± 1.0 km) and Vp/Vs (1.81 ± 0.04) values close to average extended continental crust, although results in the South Shetland Islands are significantly more heterogeneous than in the Antarctic Peninsula.

Plain Language Summary With more seismic stations than ever before, we investigate the structure of the earth beneath the Bransfield Strait (West Antarctica), a region located behind a subduction zone which features active volcanism and extension of the crust. We imaged for the first time in the region a gap in the sinking Phoenix plate which coincides with the position of the 2020–2021 Orca earthquake series. We located the two major earthquakes at the base of the crust, so we link seismicity to the flow of hot materials through the gap in the Phoenix plate and its accumulation at the base of the crust. We imaged this layer below Deception Island, and also identified a widespread area where melting probably occurs. The average thickness and seismic velocities of the crust resemble standard values of areas undergoing extension, although the South Shetland Islands are highly heterogeneous.

1. Introduction

The Bransfield Strait is a region of stretched continental crust separating the South Shetland Islands (SSI) from the Antarctic Peninsula (AP), in West Antarctica (Figure 1). The basin is an active back-arc rifting system that lies in a singular tectonic setting. The South Shetland Trench (SST), to the north-west of the SSI arc, represents the last remnant of a Mesozoic subduction zone that once occupied the whole Pacific margin of the AP and that involved the sinking of the Phoenix plate below the Antarctic plate. Subduction became gradually inactive as segments of the Antarctic-Phoenix spreading ridge entered the trench (Larter et al., 2002). Following the arrival ~3.3 Ma ago of the Hero fracture zone to the SST, spreading ceased completely in the Phoenix ridge (Livermore et al., 2000) and the Phoenix plate became fully integrated into the Antarctic plate. At this point the Bransfield Basin (BB) started opening by a combination of transtensional tectonics in the southern Scotia arc (González-Casado et al., 2000; Jin et al., 2009) and slab rollback of the Phoenix slab (e.g., Galindo-Zaldívar et al., 2004; Ibáñez et al., 1997; Jabaloy et al., 2003; Robert son Maurice et al., 2003).

The tectonic setting of the Bransfield Strait, as well as the asymmetry and segmentation of the rift, translates into a highly heterogeneous crustal structure (Barker et al., 2003; Biryol et al., 2018; Christeson et al., 2003; Parera-Portell et al., 2021). The central BB, located between Deception and Bridgeman Islands, is where extension is thought to be more prominent (Galindo-Zaldívar et al., 2004), a hypothesis also supported by recent GPS measurements (Berrocoso et al., 2016). Nowadays extension in the BB continues at a maximum rate of 7–9 mm yr^{-1} (Berrocoso et al., 2016; Taylor et al., 2008) and may be already transitioning from continental extension to oceanic spreading (e.g., Barker et al., 2003; Gràcia et al., 1996; Lawver et al., 1996). Several active volcanic edifices occur along the SW-NE rift axis, and there is widespread seismicity associated both to regional tectonics and volcanic activity (e.g., Almendros et al., 2020; Ibáñez et al., 1997; Robertson Maurice et al., 2003). A notorious example is the intense earthquake swarm that occurred in the vicinity of the Orca Seamount, an undersea volcano south of King George Island (Figure 1), from August 2020 to February 2021. The swarm

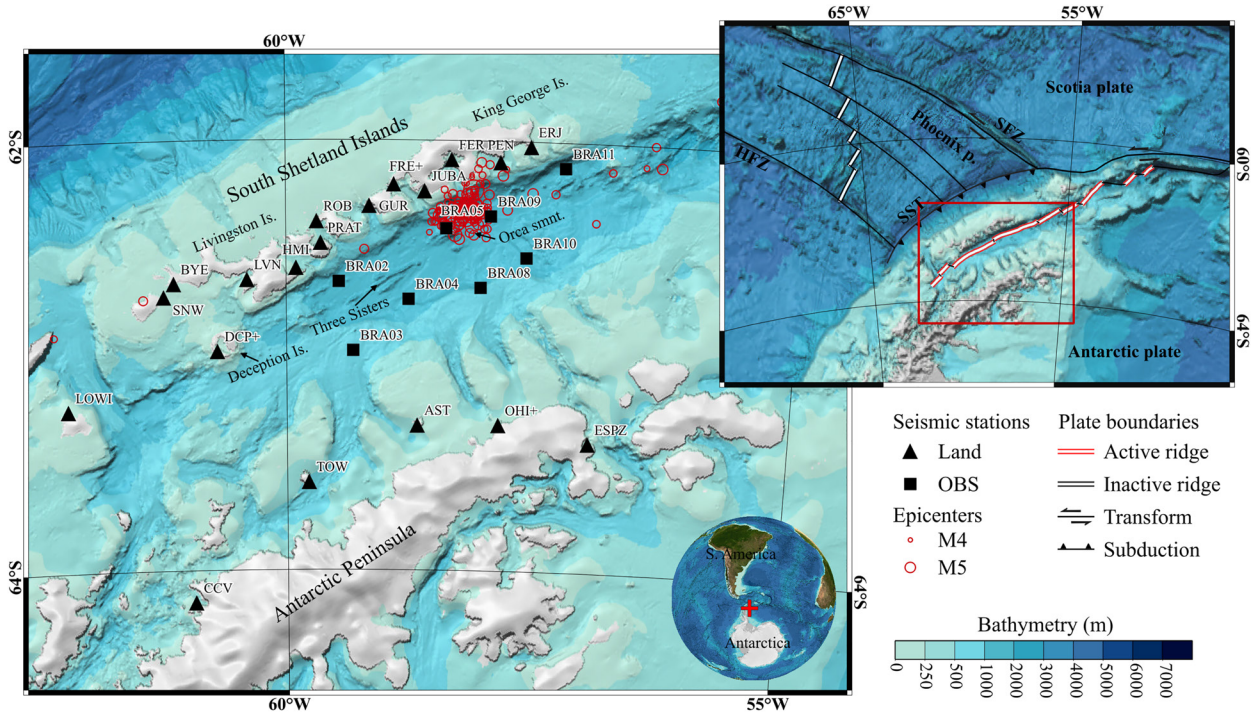

Figure 1. Location of the seismic stations and the epicenters of earthquakes (magnitude >4) from 1st August 2020 to 15th May 2021 within the Bransfield Strait, according to USGS's National Earthquake Information Center catalog. HFZ: Hero Fracture Zone, SFZ: Shackleton Fracture Zone; SST: South Shetland Trench. Maps in South Pole Azimuthal Equidistant projection. Bathymetry from GEBCO Bathymetric Compilation Group 2020 (2020).

involved ~85,000 earthquakes over 6 months (Cesca et al., 2022) including about 150 events exceeding magnitude 4.0 (USGS/NEIC, https://earthquake.usgs.gov/earthquakes/search).

Since seismic stations in the Bransfield Strait are scarce and sparsely distributed, the deployment of an amphibian seismic network during 2017–2020 under the BRAnsfield VOlcano SEISmology (BRAVOSEIS, Almendros et al., 2020) project represents a valuable opportunity to improve the current knowledge on the region's tectonics and seismicity. Here we use BRAVOSEIS seismometers in combination with past and present-day networks—summing up to 22 onshore seismic stations and eight ocean bottom seismometers (OBS)—to gather teleseismic P-wave receiver functions, which are time series of P-to-S wave conversions (Ps phases) regarded as the impulse response of the local structure beneath each recording station (Langston, 1979; Vinnik, 1977).

2. Data and Methods

Seismic data were acquired by 30 broadband seismometers from four different networks (see Figure 1 and Table S1 in Supporting Information S1): (a) 20 from the BRAVOSEIS amphibian network, including 12 onshore stations (Heit et al., 2020) and eight ocean-bottom seismometers (M. Schmidt-Aursch et al., 2021); (b) three from the permanent IAG-UGR network (Instituto Andaluz de Geofisica Universidad de Granada, 2008); (c) five belonging to the Seismic Experiment in Patagonia and Antarctica (SEPA, Wiens, 1997); and (d) two from the Antarctic Seismographic Argentinean-Italian Network (ASAIN, Istituto Nazionale di Oceanografia e di Geofisica Sperimentale, 1992).

From the available data set, events with epicentral distances between 30° and 90° from each station and magnitude greater than 5.5 were selected. Events were trimmed to keep the P-wave arrival and its coda, using a time window of −20–120 s from the P wave arrival. Only waveforms with a signal-to-noise ratio greater than 2 were kept. Waveforms were then detrended, tapered, high-pass filtered (0.5 Hz corner frequency) and decimated to 10 Hz with the previous application of an anti-aliasing filter. Finally, waveforms were rotated from the ZNE coordinate system to ZRT using the event's backazimuth and from ZRT to LQT using the theoretical incidence angle (a near-surface Vs of 3.5 km s^{-1} was assumed). Receiver functions were calculated with the iterative time-domain

deconvolution approach (Ligorría & Ammon, 1999), using 200 iterations and a Gaussian width parameter of 2.5, equivalent to a pulse width of ∼1 s. Finally, receiver functions with root-mean-square error greater than 50% were discarded. OBS required additional processing due to the unknown orientation of the horizontal components and due to the seismic waves that reverberate within the water layer that make the identification of crustal P-to-S conversions ambiguous (Audet, 2016). The orientation of the horizontal components was obtained with a Rayleigh wave arrival angle analysis (Doran & Laske, 2017), while a linear filter based on the OBS depth and reflection coefficient of the seafloor (Akuhara, 2018) was used to reduce the effect of water-layer reverberations. Only the ZNE to ZRT rotation was applied, as the presence of sediments already makes the incidence angle near-vertical.

2-D depth profiles of the BB were obtained with common-conversion-point (CCP) stacking (Yuan et al., 2000). In this seismic technique, receiver functions are backprojected from each station along a 2-D distance-depth slice divided in bins. We are using velocities from the IASP91 model (Kennett & Engdahl, 1991) for this purpose. Amplitudes are stacked in each bin that receiver functions pass through, including the first Fresnel zone, thus obtaining a cross-section of seismic velocity variations. We apply an additional phase-weighting method using the Hilbert transform of the receiver functions (Frassetto et al., 2010) to minimize the constructive stacking of noise and spurious signal.

To complement the interpretation of both the profiles and individual receiver functions, we obtained crustal thickness and Vp/Vs estimates at each onshore station with the H-κ stacking method (Zhu & Kanamori, 2000). This technique stacks the weighted amplitudes of the predicted converted wave (Ps) at the Moho and the two following multiples (PpPs and PpSS + PsPs) on a thickness-Vp/Vs space in order to find the pair of thickness and Vp/Vs values that best fit the data. We set the weighting scheme at 0.4 (Ps), 0.4 (PpPs) and 0.2 (PsPs + PpSs). Vp was fixed at 6.58 km s^{-1} in the SSI and at 6.32 km s^{-1} in the AP, following the local earth models in Robertson Maurice et al. (2003). 2-sigma errors were obtained by bootstrapping with 200 iterations (Efron & Tibshirani, 1986). Slant-stacks were also calculated, following the method in Tauzin et al. (2008) as another complementary test to check whether pulses in the data correspond to converted phases or multiples. For slant-stacking we fix a reference epicentral distance (60°) and a set of differential slownesses (δp) relative to the P-wave arrival according to which receiver functions are shortened or stretched. Data is then stacked on a time-δp space where converted phases should appear in the positive δp range. However, in such a complex tectonic setting where we expect dipping interfaces the pulses can get smeared and the ray parameter may change due to seismic waves being deflected (Bonatto, 2013).

3. Results and Discussion

The number of receiver functions yielded by each station (Table S1 in Supporting Information S1) varies greatly as a function of the deployment time, with the maximum number achieved in the permanent stations ESPZ and JUBA. Some stations were paired due to their separation being smaller than the lateral sampling of converted waves in the crust (FRE-FREI, OHI-OHIG, and DCP-DECP, respectively renamed as FRE+, OHI+, and DCP+). The backazimuth distribution of receiver functions is highly uneven, NWW and SW being the dominant directions.

Several stations (e.g., CCV, ESPZ, JUBA, and LVN) display clear signs of either dipping structure or anisotropy. CCV and DCP + required further analysis due to some unusual patterns in the receiver functions. CCV features a large negative pulse at 0 s that might suggest an incorrect orientation to N, but testing revealed its source to be the ZRT to LQT rotation. This is most probably the result of an over-rotation caused by lateral heterogeneities in the crust, but given that the rest of the pulses remain intact we chose to keep the LQT traces. In the case of DCP + there is an anomalous large pulse at time 0 s in the LQT traces. In the ZRT system this pulse at 0 s is greatly reduced and some pulses in the traces become much clearer. We suspect that such effects can be attributed to a highly complex crustal structure in the Deception Island volcano, involving many volcanic materials with different physical properties and lateral heterogeneities. In this case we chose to jointly analyze both the LQT and ZRT traces. Receiver functions are shown in Supporting Information S1 (Figures S1–S5). OBS traces, however, tend to be noisy and oscillatory and no clear conversions nor multiples can be unambiguously identified (see Figure S6 in Supporting Information S1). As a result, we were unable to estimate the crustal thickness and Vp/Vs or to include OBS data in CCP profiles. OBS are affected by complex and very local noise sources with great temporal variability (M. C. Schmidt-Aursch et al., 2022), greatly hindering the deconvolution. The role that

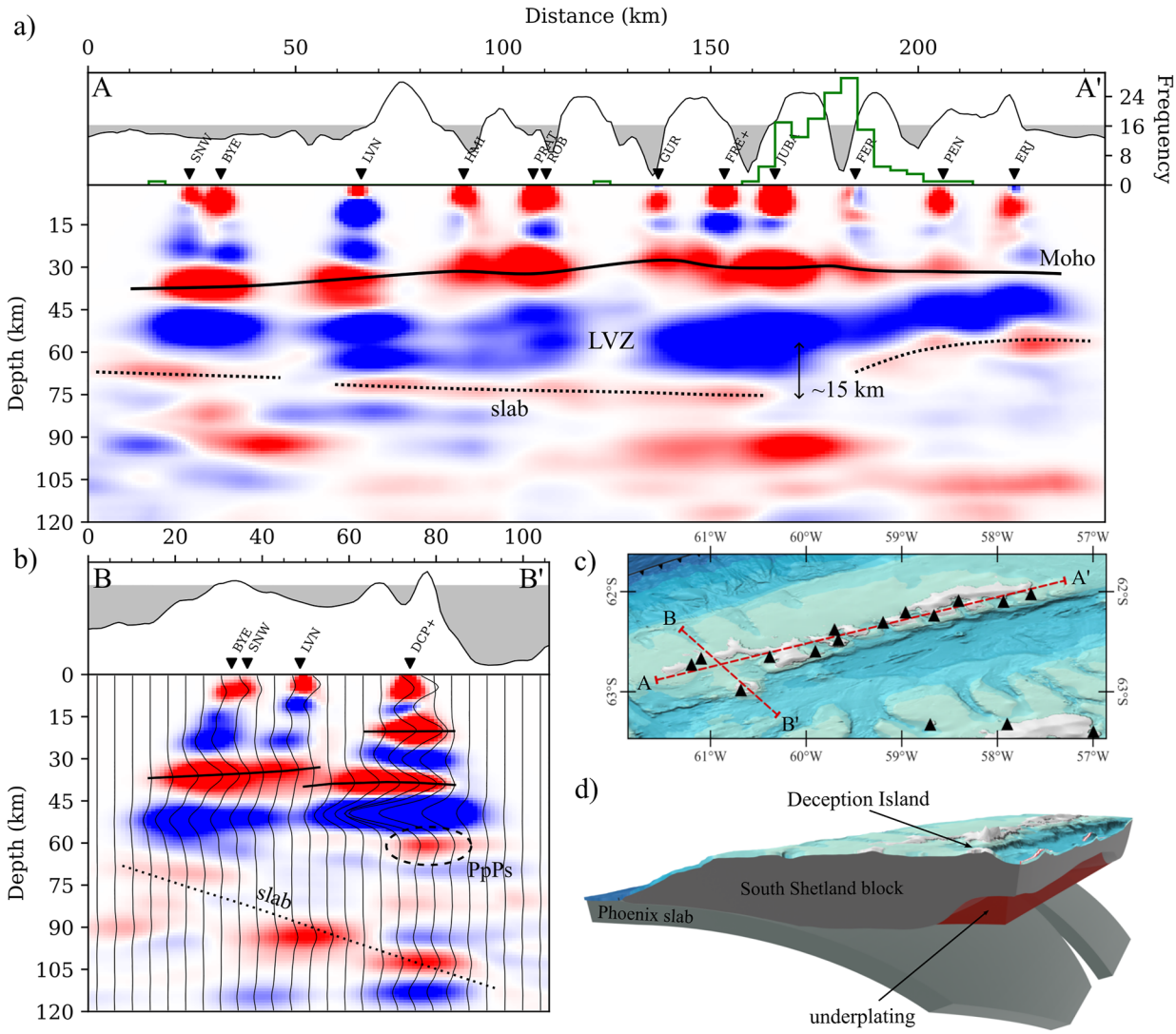

Figure 2. Common conversion point stacking profiles (a) parallel to the SSI (A.A′, frequency histogram of the Orca swarm in green) and (b) across the Bransfield Basin (B-B′). Red and blue indicate positive and negative polarity, representing a velocity increase or velocity decrease with depth, respectively. The top panels of each profile shows the topography. (c) location of the profiles; (d) model interpreted from profiles A-A′ and B-B′.

sediments play on the quality of our OBS data set is also unclear, but wave reverberations within the sediment layer are a plausible explanation for the highly oscillatory traces.

The CCP profiles in Figure 2 show a SSI block that is significantly heterogeneous, displaying a crust–mantle wedge–slab geometry as expected in such island arc context. Profile A-A′ indicates that the shallower crust in the SSI block is located in the vicinity of western King George Island, although crustal thickness in the CCP may be biased due to the selected earth model. Therefore, we estimated crustal thickness and Vp/Vs using the H-κ grid-search (Figure 3). Still, traces are highly complex and there are various secondary peaks in the H-k space, leading to high uncertainty. The thinnest crust is found near the rift axis in Deception Island (DCP+, at 15.9 ± 3.5 km), a depth that matches results in past active seismic experiments (Barker et al., 2003; Christeson et al., 2003) and ambient noise tomography by Li et al. (2021). Nevertheless, DCP + features a second Moho at approximately 40 km (see profile B-B′ in Figure 2) that we attribute to an intermediate-velocity magmatic underplating layer, as already supported by previous receiver function analyses Biryol et al. (2018) and by magma composition and inferred P-T magma formation conditions (Geyer et al., 2019). Other stations such as LVN also seem to be underlain to some degree by the underplating layer, although its pulse overlaps the Moho and is not clearly imaged. The average crustal thickness including both the SSI and the AP rises up to

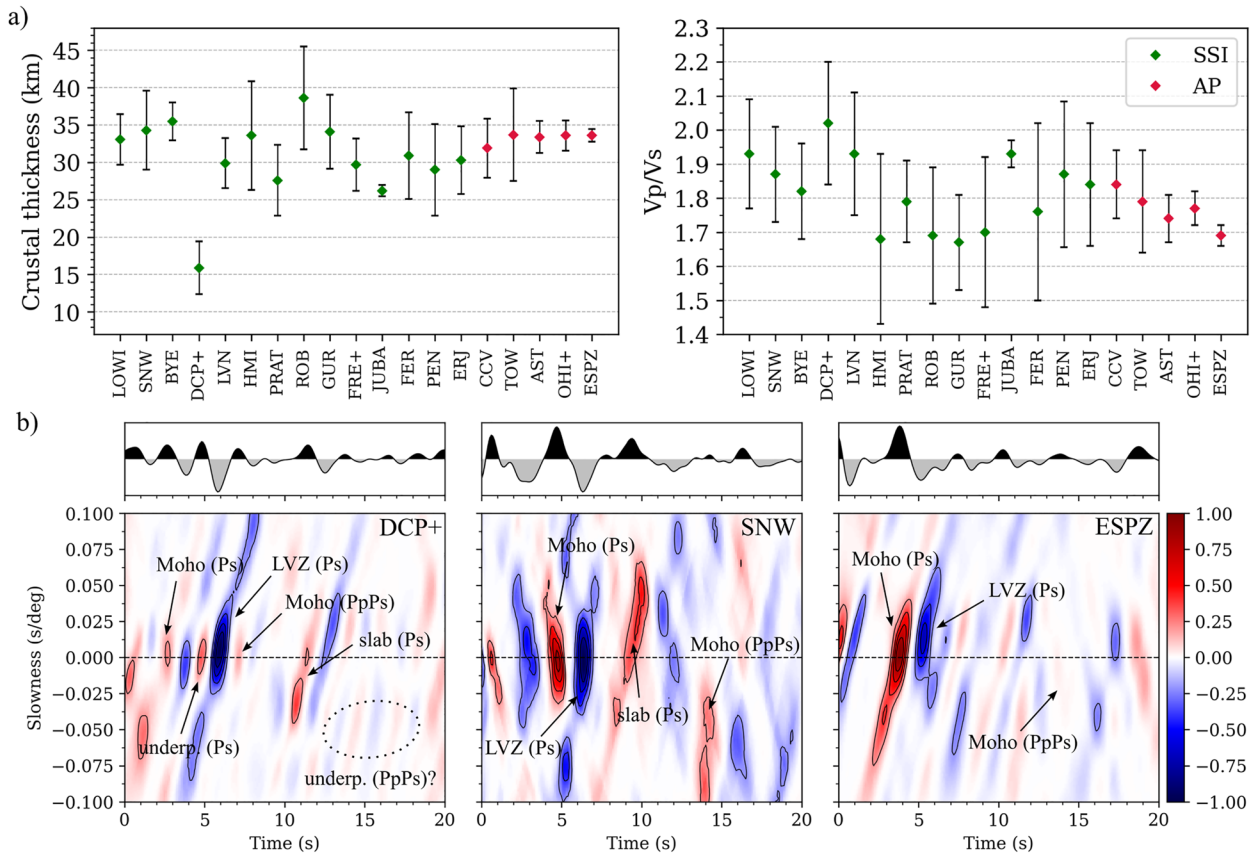

Figure 3. (a) Crustal thickness (H) and average crustal Vp/Vs ratio obtained from H-κ stacking, alongside 2-sigma uncertainty bounds. Stations are grouped by crustal block and sorted from west to east. (b) Summation trace and normalized slant stacks of three representative stations: DCP+ (radial component), SNW and ESPZ (Q component).

30.5 ± 1.0 km, in concordance with average extended continental crust (Christensen & Mooney, 1995). Excepting the DCP + outlier, we found the shallowest Moho in King George Island (JUBA, at 26.2 ± 0.8 km). Even though we could not retrieve meaningful crustal thickness and Vp/Vs estimates from OBS, the greater extension near JUBA also matches the pattern seen in Barker et al. (2003), Christeson et al. (2003), and Li et al. (2021), which also report a more asymmetrical rift in this area. The maximum Moho depth is achieved in ROB (38.6 ± 6.9 km), one of the stations closer to the forearc. In the AP, crustal thickness is more homogeneous than in the SSI and only appears to increase slightly from W to E, even though this variation falls within the 2-sigma uncertainty bounds and the number of stations is much lower.

The Vp/Vs ratio is harder to constrain than crustal thickness and commonly features high uncertainty, albeit the spatial distribution of the results offers some interesting insights. As happens with crustal thickness, the average Vp/Vs of the study area (1.81 ± 0.04) is also close to values of typical continental crust. There are, though, a number of stations where Vp/Vs rises significantly. We found the highest Vp/Vs near the rift axis, in Deception Island (2.02 ± 0.17). Such high ratio in an active volcanic island is probably indicating the presence of melts in the crust, a view supported by Muñoz-Martín et al. (2005), Ben-Zvi et al. (2009), Pedrera et al. (2012), and Geyer et al. (2019). Vp/Vs values above 1.90 are found in LOWI (1.93 ± 0.16), LVN (1.93 ± 0.19) and JUBA (1.93 ± 0.04), although those have no clear interpretation due to the lack of recent volcanism in the island arc. Such high Vp/Vs could as well be related to a highly fractured crust or to an overestimation caused by dipping structure (Lombardi et al., 2008). In the AP there seems to be a decreasing Vp/Vs tendency from W to E although, as in the case of crustal thickness, most estimates fall within the 2-sigma bounds.

H-κ stacking results allowed us to estimate the theoretical arrival times of the Moho multiples, which commonly arrive no earlier than 10 s after the direct P wave. In the CCP profiles, this time maps to depths of at least 90 km. Therefore, two potential conversions were identified between the Moho Ps and its first multiple (PpPs): (a) a wide

negative pulse in the mantle wedge that dominates the slant-stacks (see Figure 2) and (b) a sharper positive pulse attributable to the Moho of the subducted Phoenix slab. Both pulses can be identified as a conversions in the clearest slant stacks such as SNW and ESPZ, even though in most cases the dip angle of the slab probably causes the pulses to become smeared across a wide range of slownesses. The shallower wide negative pulse is seen in all stations both in the SSI and the AP, and overall seems to be the dominant feature in most individual receiver functions and also in the CCP profiles. We interpret this pulse as a conversion at a gradient-like interface where seismic velocity decreases with depth (a low velocity zone or LVZ). This LVZ probably corresponds to a region in the mantle wedge where partial melting occurs (Parera-Portell et al., 2021), and appears to stretch below all the Bransfield Strait at depths approximately between 40 and 65 km (profile A-A′ in Figure 3). The increased number of stations with respect to previous studies such as Parera-Portell et al. (2021) has also revealed lateral heterogeneity in this LVZ along the rift axis direction below the SSI: the LVZ maintains a constant thickness from LVN to JUBA, but shrinks to almost half its thickness from JUBA eastwards. This is also accompanied by a depth variation of the pulse below, that is, the Moho of the Phoenix slab.

The depth of the slab also changes west to east: it deepens gradually from ∼65 km in SNW and BYE to ∼75 km in the LVN–JUBA section, and suddenly rises to ∼60 km east of JUBA. We attribute the ∼15 km slab step between JUBA and FER to slab tearing occurring along an ancient fracture zone in the Phoenix plate associated to the extinct Phoenix–Antarctic ridge (see Figure 1). The position of the tear appears to mark the transition between regions with different degrees of extension, with a deeper Moho and a more symmetrical rift toward the SW (Barker et al., 2003; Li et al., 2021). The location of some topographic features also evidences this segmentation, such a ∼8 km northwards offset of the Bransfield ridge—and also of the associated magnetic and gravity anomalies (Almendros et al., 2020; Espinoza et al., 2023)—between Three Sisters and Orca seamounts. Volcanic edifices east of the slab tear may also appear much closer to the SSI than in any other section of the basin. However, although the deeper slab segment suggests an increased rollback rate in the SW sector, the thinnest crust is found directly above the tear or on top of the shallower NE segment (Li et al., 2021), which is also slightly older (20–25 Ma) than the SW segment (10–15 Ma) at the SST contact (Larter & Barker, 1991). The slab depth difference then can not be linked to a density contrast between the slab segments, but it could be attributed to increased slab pull in the SW segment, which is attached to a large portion of the Phoenix slab deeper to the SW, as imaged by seismic tomography (Lloyd et al., 2020). This hypothesis also implies that the greater extension in the eastern Central Bransfield Basin (CBB) is due to the additional contribution of transtension at the Scotia-Antarctic plate boundary, as supported in González-Casado et al. (2000). We were able to estimate the dip angle of the SW slab segment under LVN at 30°–40°, by comparing the position at which receiver functions with different ray paths pierced the discontinuity. Further into the basin the slab eventually reaches a very steep dip angle of up to 70°, according to Park et al. (2012) and Lloyd et al. (2020), and may arrive at the mantle transition zone below the AP (Parera-Portell et al., 2021).

Remarkably, the 2020–2021 earthquake swarm south of King George Island occurs on top of the inferred slab tear (Figure 3) and where the Moho is shallowest (10–12 km), according to Barker et al. (2003) and Li et al. (2021). Moment tensor estimates are available for 31 earthquakes of the Orca swarm from the Global Centroid Moment Tensor (GCMT) catalog (Dziewonski et al., 1981; Ekström et al., 2012), with magnitudes between 4.8 and 5.9, and for 84 earthquakes above magnitude 4.1 from Cesca et al. (2022). The solutions show strike-slip and normal faulting with NW-SE orientation of the tensional principal axis of the focal mechanisms. We use stress tensor inversion (Gephart, 1990) to quantify the style and orientation of local deformation from the GCMT solutions. Inversion yields the minimum principal stress σ_3 in direction N135°E, with sub-horizontal plunge angle of 9°. According to the GCMT focal mechanisms and average stress tensor, the Orca swarm has no apparent relation with slab tearing, but rather reflects back-arc extension in NW-SE direction, perpendicular to the SST, and has to be associated to a major magmatic intrusion. We analyze source depths to support this assignation.

Centroid depth estimates for the Orca swarm in the GCMT catalog range from 12 km (fixed depths in some cases) to 24 km, while depths are mostly shallower than 15 km in Cesca et al. (2022), with the strongest events near 9 km depth. These estimates place the swarm within the thinned continental crust in the second case, but below the local continental Moho in the first, suggesting seismicity within the underplating layer, even though with our current data set we can not constrain the morphology and extent of the underplating layer at this location. To verify depth estimates and the environment in which earthquakes occur, we model primary surface reflections in vertical component P-waveforms recorded between 30° and 90° distance. We select waveforms with adequate signal-to-noise ratio for these moderate magnitude events, excluding the most complicated waveforms that may

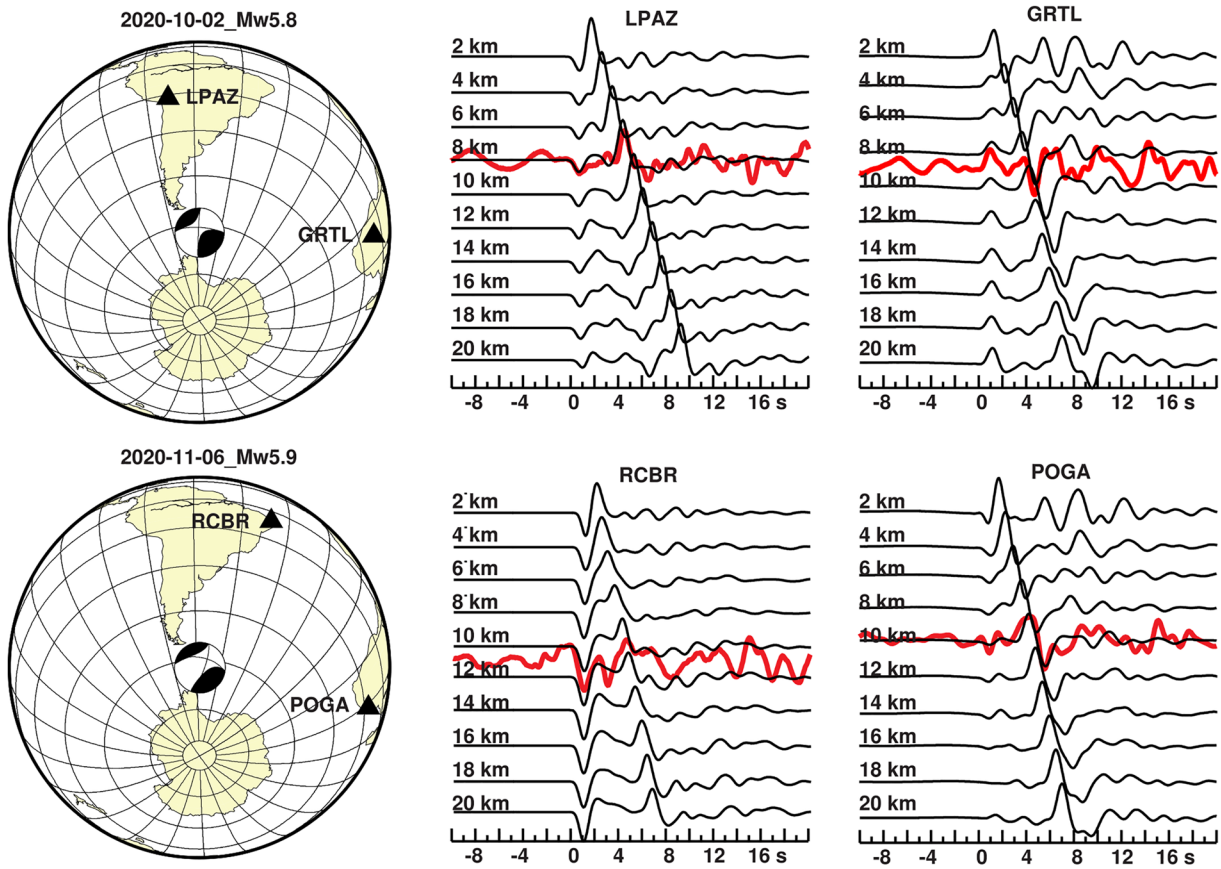

Figure 4. Comparison of synthetic waveforms at different depths (black lines) and observed seismograms (red lines) for the earthquakes on 2nd October 2020 (Mw 5.8, top) and 6th November 2020 (Mw 5.9, bottom). All waveforms are normalized to unit amplitude. Waveforms at stations in South America (LPAZ, RCBR) and southern Africa (GRTL, POGA) show best coincidence for crustal source depths around 10 km.

be affected by local Earth structure on the receiver side. We decided to not model water layer depth phases due to the significant epicenter uncertainties in combination with rather abrupt bathymetry. Synthetic waveforms are obtained from Axisymmetric Spectral Element Modeling (Nissen-Meyer et al., 2014; van Driel et al., 2015), and retrieved through the Syngine tool (Krischer et al., 2017). We assume moment tensor sources according to the global CMT project, the global ak135f velocity model (Kennett et al., 1995) and density and attenuation from Montagner and Kennett (1996). This velocity model assumes crustal P-wave velocity of 5.8 km.s^{-1} (lower than the average regional P-wave speed used in RF modeling) which may account for the presence of sediments in the axial zone of the Bransfield Rift.

Focal depth modeling from teleseismic waveforms indicates shallow depths (8–11 km) for the two largest earthquakes (Mw 5.8 and 5.9, Figure 4). In particular, we achieve proper matches for the sP phase, which is the dominant depth phase in African and South American stations due to the proximity to the nodal planes of P-wave radiation. Modeling is less successful for southern station azimuths, presumably due to the omission of a water layer. The location of seismicity within an area of highly stretched crust (Barker et al., 2003; Li et al., 2021) suggest attributing the earthquakes to magma movement, a view also shared by Cesca et al. (2022). The integration of the Orca swarm into the structural context from receiver function analysis suggests an origin from an episode of magmatic underplating in this sector, where magmatic intrusions and deep crustal seismicity occur according to the regional stress field. Even though we have no direct evidence for an underplating layer below Orca with our current data set, joint geophysical and petrological models (Yegorova et al., 2010) and wide-angle seismic surveys (Christeson et al., 2003; Janik et al., 2014) support the presence of a widespread high-velocity body underplating the crust of the BB. Moreover, Orca may be analogous to Deception Island, where underplating of hot mantle materials is thought to be partly caused by the opening of a slab window to the east of the HFZ (Biryol et al., 2018). Below Orca, the slab tear also allows direct mantle flow through the gap and may contribute to a similar case of underplating.

4. Conclusions

The addition of the BRAVOSEIS seismic network to the existing seismic data set of the Bransfield Strait allowed us to perform the highest-resolution receiver function analysis of the region to date. Even though the OBS did not provide convenient receiver functions, we imaged for the first time a slab tear under the CBB and lateral depth changes of a low-velocity layer in the mantle wedge at 40–65 km. We speculate that slab tearing occurs along an ancient fracture zone in the Phoenix plate that reaches the trench. The tear causes the slab to become 15 km shallower to the east, and agrees well with changes in magnetic and gravimetric anomalies, bathymetry and Moho topography. We also found that the epicenters of the 2020–2021 Orca swarm coincide with the area where slab tearing occurs, but we could not find any direct mechanical link between both events. Instead, we propose that the Orca swarm may have been triggered by active magmatic underplating, facilitated by hot mantle flow through the slab tear into the basin. We imaged an underplating layer between 15 and 40 km under Deception Island, which we think is an analogous case and may reflect the lithospheric structure of the areas closer to the rift axis. We estimated the Moho depth and Vp/Vs ratio with the H-κ stacking method and found that, generally, the crustal thickness and Vp/Vs ratios are close to typical extended continental crust (Christensen & Mooney, 1995), averaging 30.5 $\pm$ 1.0 km and 1.81 $\pm$ 0.04, respectively. DCP+, located in Deception Island, is the station that deviates the most from the average values, displaying a Moho depth of 15.9 $\pm$ 3.5 km and Vp/Vs of 2.02 $\pm$ 0.17 that likely reflect the accumulation of melts in the crust.

Data Availability Statement

Data from the ASAIN (AI, Istituto Nazionale di Oceanografia e di Geofisica Sperimentale, 1992), SEPA (XB, Wiens, 1997) and the IAG-UGR (B6, Instituto Andaluz de Geofisica Universidad de Granada, 2008) networks are accessible through IRIS DMC. Data from BRAVOSEIS onshore (5M, Heit et al., 2020) and offshore (ZX, M. Schmidt-Aursch et al., 2021) networks are archived at the GEOFON Data Centre and the PANGAEA Open Access library, respectively. Teleseismic waveforms for depth determination were downloaded through the IRIS Wilber 3 system.

Acknowledgments
We are grateful to the staff involved in the Antarctic campaigns run by the Instituto Andaluz de Geofísica—Universidad de Granada (that manages the IAG-UGR network) and in the BRAVOSEIS experiment and the ASAIN and SEPA seismic networks. This work was funded by Spanish national projects PID2019-109608GB-100/SRA/10.13039/501100011033 and CMT2016-77315-R, the Andalusian regional project A-RNM-421-UGR18 and the FPI Grant PRE2020-092556 (funded by MCIN/AEI/10.13039/501100011033 and the European Social Fund). We acknowledge work on free software SAC (Goldstein & Snoke, 2005), QGIS and Blender. Last but not least, thanks to the reviewers and editor for their suggestions and help.

References

Akuhara, T. (2018). *Fluid distribution along the Nankai-trough megathrust fault off the Kii peninsula*. Springer Theses. https://doi.org/10.1007/978-981-10-8174-3

Almendros, J., Wilcock, W., Soule, D., Teixidó, T., Vizcaíno, L., Ardanaz, O., et al. (2020). BRAVOSEIS: Geophysical investigation of rifting and volcanism in the Bransfield Strait, Antarctica. *Journal of South American Earth Sciences*, *104*, 102834. https://doi.org/10.1016/j.jsames.2020.102834

Audet, P. (2016). Receiver functions using OBS data: Promises and limitations from numerical modelling and examples from the Cascadia initiative. *Geophysical Journal International*, *205*(3), 1740–1755. https://doi.org/10.1093/gji/ggw111

Barker, D. H., Christeson, G. L., Austin, J. A., & Dalziel, I. W. (2003). Backarc basin evolution and cordilleran orogenesis: Insights from new ocean-bottom seismograph refraction profiling in Bransfield Strait, Antarctica. *Geology*, *31*(2), 107. https://doi.org/10.1130/0091-7613(2003)031(0107:bbeaco)2.0.co;2

Ben-Zvi, T., Wilcock, W. S. D., Barclay, A. H., Zandomeneghi, D., Ibáñez, J. M., & Almendros, J. (2009). The P-wave velocity structure of Deception Island, Antarctica, from two-dimensional seismic tomography. *Journal of Volcanology and Geothermal Research*, *180*(1), 67–80. https://doi.org/10.1016/j.jvolgeores.2008.11.020

Berrocoso, M., Fernández-Ros, A., Prates, G., García, A., & Kraus, S. (2016). Geodetic implications on block formation and geodynamic domains in the South Shetland Islands, Antarctic Peninsula. *Tectonophysics*, *666*, 211–219. https://doi.org/10.1016/j.tecto.2015.10.023

Biryol, C. B., Lee, S. J., Lees, J. M., & Shore, M. J. (2018). Lithospheric structure of an incipient rift basin: Results from receiver function analysis of Bransfield Strait, NW Antarctic Peninsula. *Polar Science*, *16*, 47–58. https://doi.org/10.1016/j.polar.2018.02.003

Bonatto, L. (2013). Novel technique to detect seismic signals and its application to map upper-mantle discontinuities beneath Iberia (PhD thesis). *Universidad de Granada*.

Cesca, S., Sugan, M., Rudzinski, Ł., Vajedian, S., Niemz, P., Plank, S., et al. (2022). Massive earthquake swarm driven by magmatic intrusion at the Bransfield Strait, Antarctica. *Communications Earth & Environment*, *3*(1), 89. https://doi.org/10.1038/s43247-022-00418-5

Christensen, N. I., & Mooney, W. D. (1995). Seismic velocity structure and composition of the continental crust: A global view. *Journal of Geophysical Research*, *100*(B6), 9761–9788. https://doi.org/10.1029/95jb00259

Christeson, G. L., Barker, D. H. N., Austin, J. A., & Dalziel, I. W. D. (2003). Deep crustal structure of Bransfield Strait: Initiation of a back arc basin by rift reactivation and propagation. *Journal of Geophysical Research*, *108*(B10), 2492. https://doi.org/10.1029/2003jb002468

Doran, A. K., & Laske, G. (2017). Ocean-bottom seismometer instrument orientations via automated Rayleigh-wave arrival-angle measurements. *Bulletin of the Seismological Society of America*, *107*(2), 691–708. https://doi.org/10.1785/0120160165

Dziewonski, A. M., Chou, T.-A., & Woodhouse, J. H. (1981). Determination of earthquake source parameters from waveform data for studies of global and regional seismicity. *Journal of Geophysical Research*, *86*(B4), 2825–2852. https://doi.org/10.1029/jb086ib04p02825

Efron, B., & Tibshirani, R. (1986). Bootstrap methods for standard errors, confidence intervals, and other measures of statistical accuracy. *Statistical Science*, *1*(1), 54–75. https://doi.org/10.1214/ss/1177013815

Ekström, G., Nettles, M., & Dziewoński, A. (2012). The global CMT project 2004–2010: Centroid-moment tensors for 13,017 earthquakes. *Physics of the Earth and Planetary Interiors*, *200*, 1–9. https://doi.org/10.1016/j.pepi.2012.04.002

Espinoza, J. A., Cahuana, N. G., Martillo-Bustamante, C. E., & González-Bonilla, M. (2023). Bransfield Strait and South Shetland Islands sedimentary basement and upper crustal structure: An analysis of gravity and magnetic data at the northwestern area of the Antarctic Peninsula. *Tectonophysics*, *852*, 229771. https://doi.org/10.1016/j.tecto.2023.229771

Frassetto, A., Zandt, G., Gilbert, H., Owens, T. J., & Jones, C. H. (2010). Improved imaging with phase-weighted common conversion point stacks of receiver functions. *Geophysical Journal International*, https://doi.org/10.1111/j.1365-246x.2010.04617.x

Galindo-Zaldívar, J., Gamboa, L., Maldonado, A., Nakao, S., & Bochu, Y. (2004). Tectonic development of the Bransfield Basin and its prolongation to the South Scotia Ridge, northern Antarctic Peninsula. *Marine Geology*, *206*(1–4), 267–282. https://doi.org/10.1016/j.margeo.2004.02.007

GEBCO Bathymetric Compilation Group 2020. (2020). *The GEBCO 2019 Grid—A continuous terrain model of the global oceans and land*. British Oceanographic Data Centre, National Oceanography Centre. https://doi.org/10.5285/A29C5465-B138-234D-E053-6C86ABC040B9

Gephart, J. W. (1990). FMSI: A FORTRAN program for inverting fault/slickenside and earthquake focal mechanism data to obtain the regional stress tensor. *Computers & Geosciences*, *16*(7), 953–989. https://doi.org/10.1016/0098-3004(90)90105-3

Geyer, A., Álvarez-Valero, A. M., Gisbert, G., Aulinas, M., Hernández-Barreña, D., Lobo, A., & Marti, J. (2019). Deciphering the evolution of Deception Island's magmatic system. *Scientific Reports*, *9*(1), 373. https://doi.org/10.1038/s41598-018-36188-4

Goldstein, P., & Snoke, A. (2005). *SAC availability for the IRIS community*. Incorporated Institutions for Seismology Data Management Center Electronic Newsletter.

González-Casado, J. M., Giner Robles, J. L., & López-Martínez, J. (2000). Bransfield Basin, Antarctic Peninsula: Not a normal backarc basin. *Geology*, *28*(11), 1043. https://doi.org/10.1130/0091-7613(2000)28⟨1043:bbapna⟩2.0.co;2

Gràcia, E., Canals, M., Farràn, M., Prieto, M. J., & Sorribas, J., & Gebra Team. (1996). Morphostructure and evolution of the central and eastern Bransfield Basins (NW Antarctic Peninsula). *Marine Geophysical Researches*, *18*(2–4), 429–448. https://doi.org/10.1007/bf00286088

Heit, B., Yuan, X., Almendros, J., Abella, R., Carmona, E., Aguí, F., & Carrión, P. (2020). Bravoseis onshore seismic array [Dataset]. GFZ Data Services. https://doi.org/10.14470/0Z7563857972

Ibáñez, J. M., Morales, J., Alguacil, G., Almendros, J., Oritz, R., & Del Pezzo, E. (1997). Intermediate-focus earthquakes under South Shetland Islands (Antarctica). *Geophysical Research Letters*, *24*(5), 531–534. https://doi.org/10.1029/97gl00314

Instituto Andaluz de Geofisica Universidad de Granada. (2008). Bransfield Strait seismic network [Dataset]. International Federation of Digital Seismograph Networks. https://doi.org/10.7914/SN/B6

Istituto Nazionale di Oceanografia e di Geofisica Sperimentale. (1992). Antarctic Seismographic Argentinean Italian network - OGS [Dataset]. International Federation of Digital Seismograph Networks. https://doi.org/10.7914/SN/AI

Jabaloy, A., Balanyá, J. C., Barnolas, A., Galindo-Zaldívar, J., Hernández-Molina, F. J., Maldonado, A., et al. (2003). The transition from an active to a passive margin (SW end of the South Shetland Trench, Antarctic Peninsula). *Tectonophysics*, *366*(1–2), 55–81. https://doi.org/10.1016/s0040-1951(03)00060-x

Janik, T., Grad, M., Guterch, A., & Środa, P. (2014). The deep seismic structure of the Earth's crust along the Antarctic Peninsula—A summary of the results from Polish geodynamical expeditions. *Global and Planetary Change*, *123*, 213–222. https://doi.org/10.1016/j.gloplacha.2014.08.018

Jin, Y. K., Lee, J., Hong, J. K., & Nam, S. H. (2009). Is subduction ongoing in the South Shetland Trench, Antarctic Peninsula?: New constraints from crustal structures of outer trench wall. *Geosciences Journal*, *13*(1), 59–67. https://doi.org/10.1007/s12303-009-0005-5

Kennett, B. L. N., & Engdahl, E. R. (1991). Traveltimes for global earthquake location and phase identification. *Geophysical Journal International*, *105*(2), 429–465. https://doi.org/10.1111/j.1365-246x.1991.tb06724.x

Kennett, B. L. N., Engdahl, E. R., & Buland, R. (1995). Constraints on seismic velocities in the Earth from traveltimes. *Geophysical Journal International*, *122*(1), 108–124. https://doi.org/10.1111/j.1365-246x.1995.tb03540.x

Krischer, L., Hutko, A. R., van Driel, M., Stähler, S., Bahavar, M., Trabant, C., & Nissen-Meyer, T. (2017). On-demand custom broadband synthetic seismograms. *Seismological Research Letters*, *88*(4), 1127–1140. https://doi.org/10.1785/0220160210

Langston, C. A. (1979). Structure under Mount Rainier, Washington, inferred from teleseismic body waves. *Journal of Geophysical Research*, *84*(B9), 4749. https://doi.org/10.1029/jb084ib09p04749

Larter, R. D., & Barker, P. F. (1991). Effects of ridge crest-trench interaction on Antarctic-phoenix spreading: Forces on a young subducting plate. *Journal of Geophysical Research*, *96*(B12), 19583–19607. https://doi.org/10.1029/91jb02053

Larter, R. D., Cunningham, A. P., Barker, P. F., Gohl, K., & Nitsche, F. O. (2002). Tectonic evolution of the Pacific margin of Antarctica 1. Late Cretaceous tectonic reconstructions. *Journal of Geophysical Research*, *107*(B12), EPM5–1–EPM5–19. https://doi.org/10.1029/2000jb000052

Lawver, L., Sloan, B., Barker, D., Ghidella, M., Von Herzen, R., Keller, R., et al. (1996). Distributed, active extension in Bransfield Basin Antarctic Peninsula: Evidence from multibeam bathymetry. *Geological Society of America Today*, *6*(11), 1–6.

Li, W., Yuan, X., Heit, B., Schmidt-Aursch, M. C., Almendros, J., Geissler, W. H., & Chen, Y. (2021). Back-arc extension of the Central Bransfield Basin induced by ridge–trench collision: Implications from ambient noise tomography and stress field inversion. *Geophysical Research Letters*, *48*(21), e2021GL095032. https://doi.org/10.1029/2021gl095032

Ligorría, J., & Ammon, C. (1999). Iterative deconvolution and receiver-function estimation. *Bulletin of the Seismological Society of America*, *89*(5), 1395–1400. https://doi.org/10.1785/bssa0890051395

Livermore, R., Balanyá, J. C., Maldonado, A., Martínez, J. M., Rodríguez-Fernández, J., Sanz de Galdeano, C., et al. (2000). Autopsy on a dead spreading center: The Phoenix Ridge, Drake Passage, Antarctica. *Geology*, *28*(7), 607. https://doi.org/10.1130/0091-7613(2000)28⟨607:aoadsc⟩2.0.co;2

Lloyd, A. J., Wiens, D. A., Zhu, H., Tromp, J., Nyblade, A. A., Aster, R. C., et al. (2020). Seismic structure of the Antarctic upper mantle imaged with adjoint tomography. *Journal of Geophysical Research: Solid Earth*, *125*(3). https://doi.org/10.1029/2019jb017823

Lombardi, D., Braunmiller, J., Kissling, E., & Giardini, D. (2008). Moho depth and Poisson's ratio in the Western–Central Alps from receiver functions. *Geophysical Journal International*, *173*(1), 249–264. https://doi.org/10.1111/j.1365-246X.2007.03706.x

Montagner, J., & Kennett, B. L. N. (1996). How to reconcile body-wave and normal-mode reference Earth models. *Geophysical Journal International*, *125*(1), 229–248. https://doi.org/10.1111/j.1365-246x.1996.tb06548.x

Muñoz-Martín, A., Catalán, M., Martín-Dávila, J., & Carbó, A. (2005). Upper crustal structure of Deception Island area (Bransfield Strait, Antarctica) from gravity and magnetic modelling. *Antarctic Science*, *17*(2), 213–224. https://doi.org/10.1017/s0954102005002622

Nissen-Meyer, T., van Driel, M., Stähler, S. C., Hosseini, K., Hempel, S., Auer, L., et al. (2014). AxiSEM: Broadband 3-D seismic wavefields in axisymmetric media. *Solid Earth*, *5*(1), 425–445. https://doi.org/10.5194/se-5-425-2014

Parera-Portell, J. A., de Lis Mancilla, F., Morales, J., Almendros, J., & Jiménez-Morales, V. (2021). Structure of the crust and upper mantle beneath the Bransfield Strait (Antarctica) using P receiver functions. *Tectonophysics*, *802*, 228744. https://doi.org/10.1016/j.tecto.2021.228744

Park, Y., Kim, K.-H., Lee, J., Yoo, H. J., & Plasencia, L. M. P. (2012). P-wave velocity structure beneath the northern Antarctic Peninsula: Evidence of a steeply subducting slab and a deep-rooted low-velocity anomaly beneath the central Bransfield Basin. *Geophysical Journal International*, https://doi.org/10.1111/j.1365-246x.2012.05684.x

Pedrera, A., Ruiz-Constán, A., Heredia, N., Galindo-Zaldívar, J., Bohoyo, F., Marín-Lechado, C., et al. (2012). The fracture system and the melt emplacement beneath the Deception Island active volcano, South Shetland Islands, Antarctica. *Antarctic Science*, *24*(2), 173–182. https://doi.org/10.1017/s0954102011000794

Robertson Maurice, S. D., Wiens, D. A., Shore, P. J., Vera, E., & Dorman, L. M. (2003). Seismicity and tectonics of the South Shetland Islands and Bransfield Strait from a regional broadband seismograph deployment. *Journal of Geophysical Research*, *108*(B10), 2461. https://doi.org/10.1029/2003jb002416

Schmidt-Aursch, M., Almendros, J., & Geissler, W. H. (2021). Project BRAVOSEIS: DEPAS ocean-bottom seismometer operations in the Bransfield Strait in 2019-2020 [Dataset]. PANGAEA—Data Publisher for Earth and Environmental Science. https://doi.org/10.1594/PANGAEA.934130

Schmidt-Aursch, M. C., & Geissler, W., & BRAVOSEIS working group. (2022). Noise characteristics of ocean-bottom seismometer data. In *BRAVOSEIS workshop* (p. 1). Online.

Tauzin, B., Debayle, E., & Wittlinger, G. (2008). The mantle transition zone as seen by global Pds phases: No clear evidence for a thin transition zone beneath hotspots. *Journal of Geophysical Research*, *113*(B8), B08309. https://doi.org/10.1029/2007jb005364

Taylor, F. W., Bevis, M. G., Dalziel, I. W. D., Smalley, R., Frohlich, C., Kendrick, E., et al. (2008). Kinematics and segmentation of the South Shetland Islands-Bransfield Basin system, northern Antarctic Peninsula. *Geochemistry, Geophysics, Geosystems*, *9*(4), Q04035. https://doi.org/10.1029/2007gc001873

van Driel, M., Krischer, L., Stähler, S. C., Hosseini, K., & Nissen-Meyer, T. (2015). Instaseis: Instant global seismograms based on a broadband waveform database. *Solid Earth*, *6*(2), 701–717. https://doi.org/10.5194/se-6-701-2015

Vinnik, L. (1977). Detection of waves converted from P to SV in the mantle. *Physics of the Earth and Planetary Interiors*, *15*(1), 39–45. https://doi.org/10.1016/0031-9201(77)90008-5

Wiens, D. A. (1997). Seismic experiment in Patagonia and Antarctica, A broadband study of the tectonics and structure of the Antarctic Peninsula and Scotia Sea Regions [Dataset]. International Federation of Digital Seismograph Networks. https://doi.org/10.7914/SN/XB_1997

Yegorova, T., Bakhmutov, V., Janik, T., & Grad, M. (2010). Joint geophysical and petrological models for the lithosphere structure of the Antarctic Peninsula continental margin. *Geophysical Journal International*, *184*(1), 90–110. https://doi.org/10.1111/j.1365-246x.2010.04867.x

Yuan, X., Sobolev, S., Kind, R., Oncken, O., Bock, G., Asch, G., et al. (2000). Subduction and collision processes in the Central Andes constrained by converted seismic phases. *Nature*, *408*(6815), 958–961. https://doi.org/10.1038/35050073

Zhu, L., & Kanamori, H. (2000). Moho depth variation in southern California from teleseismic receiver functions. *Journal of Geophysical Research*, *105*(B2), 2969–2980. https://doi.org/10.1029/1999jb900322